ANGULAR RATE GYROSCOPE WITH DUAL ANCHOR SUPPORT

Gary J. O'Brien[*,+], David J. Monk[+], and Khalil Najafi[*]

[*]**University of Michigan**
Center for Wireless Integrated Microsystems
1301 Beal Ave
Ann Arbor, MI 48109-2122

[+]**Motorola Inc.**
Sensor Products Division
Sensor Development Engineering Group
Tempe, AZ 85284

ABSTRACT

A low-cost high yield surface micromachined gyroscope is presented with a decoupled drive and sense proof mass. A dual anchor approach is described using folded beam springs and a torsion post to significantly reduce the drive proof mass out of plane deflection while maintaining a comparatively low rotational mechanical restoring force. The Z-axis (vertical) proof mass suspension spring constant was increased from 7.86 [N/m] to 251[kN/m] with the addition of the central torsion post. Vertical stiction was eliminated from the design using the dual anchor scheme for the proof mass and a triply clamped beam approach for the fixed electrostatic drive/sense beams. The increase in the Z-axis spring constant of the fixed triply clamped beams is greater than 128X as compared to singly clamped cantilever beams of equal length. In addition, a differential capacitance measurement scheme is presented which rejects undesired proof mass linear acceleration error at the sensor. The sense mode resonant frequency was measured at 44.96 [kHz] with a quality factor Q of 225 in a 3 mtorr ambient. Angular rate resolution was measured at 3.8 [deg/s] in a 20 [Hz] bandwidth.

INTRODUCTION

During the past decade a great deal of research has been performed on MEMS based vibratory gyroscopes for intended use in automotive and inertial navigation applications. Angular rate sensors (gyroscopes) have been implemented using vibrating rings [**1**,**2**], prismatic beams [**3**], tuning forks [**4**-**6**], and torsion [**7**,**8**] oscillation. Significant capacitance based measurement error for the tuning fork and torsional rate gyroscopes is caused by undesired mechanical and electrostatic coupling with the proof mass drive and sense modes. Mechanical decoupling of the drive and sense modes using a torsion beam spring has been previously demonstrated [**8**] with significant reduction of undesirable nonlinear rate output characteristics reported. The Dual Anchor Angular Rate (DAART) sensor, shown in Figure 1, utilizes torsion oscillation with mechanically decoupled drive and sense proof mass modes using a modified torsion spring as shown in Figure 2. The dual anchor design significantly increases the Z-axis spring constant while maintaining a comparatively low rotational mechanical restoring force about the Z-axis. This is accomplished using a 2μm diameter torsion post anchored to the substrate in addition to folded beam springs which suppress precession of the proof mass during rotational (torsion) oscillation, as shown in Figure 3. A 21% increase in the theoretical folded beam spring mechanical restoring force is attributed to inclusion of the torsion post anchor proof mass displacement around the z-axis. Neglecting the proof mass stiffness, the z-axis system spring constant is significantly improved from 7.86 [N/m] to 251[kN/m], with the torsion post included.

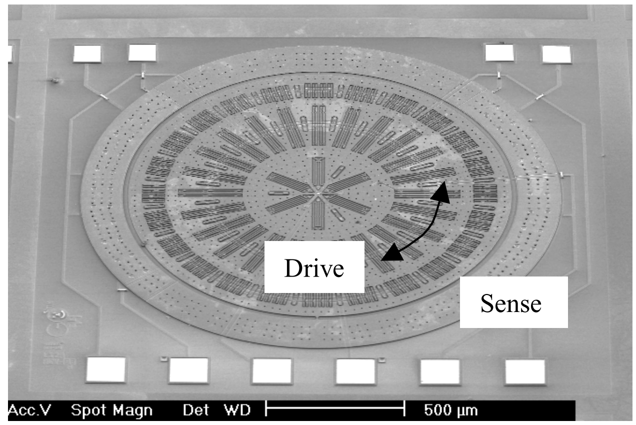

Figure 1*. DAART Sensor Decoupled Inner Drive and Outer Sense Ring Proof Mass*

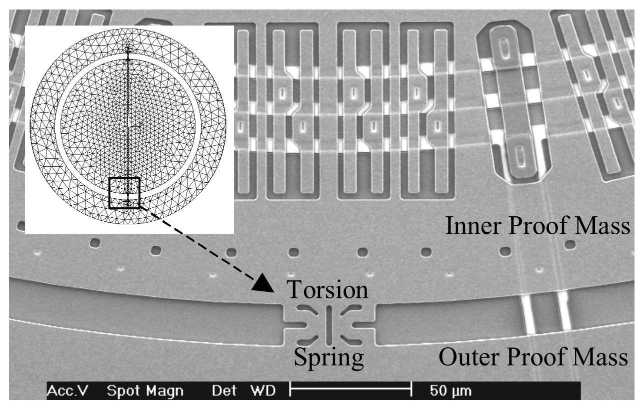

Figure 2*. Decoupled Inner Drive and Outer Sense Proof Mass Torsion Spring*

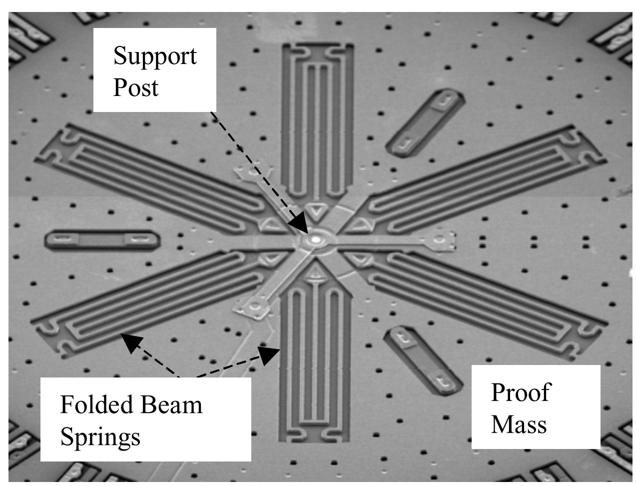

Figure 3*. DAART Sensor Central Spring Suspension*

0-9640024-4-2/hh2002/$20©2002TRF
DOI 10.31438/trf.hh2002.71

SENSOR OPERATION

The torsional drive and sense modes are intentionally mismatched to reduce quadrature error [**6**] during excitation. The inner ring is electrostatically driven at the resonant frequency of the outer sense proof mass, providing the coupling energy for Coriolis acceleration measurement. Vibratory gyroscopes sense angular rate based on the Coriolis acceleration measurement defined by the cross product of the mass velocity *v*, and the rotation rate Ω, as given by Eq. 1.

$$a_{Coriolis} = 2v \times \Omega \quad (1)$$

The outer proof mass is segmented into quadrants where the effective mass is approximately half the total mass. Coriolis force is defined by the product of the effective outer proof mass *m* and Coriolis acceleration as given by Eq. 2.

$$F_{Coriolis} = 2mv \times \Omega \quad (2)$$

The Coriolis force couple causes a rotation of the outer sense ring for a counter clockwise rotation as shown in Figure 4.

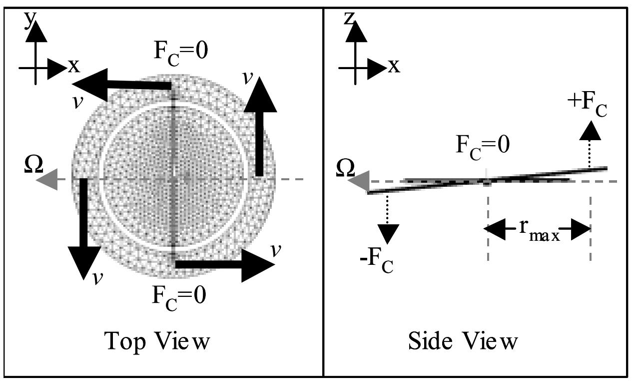

***Figure 4**. Outer Proof Mass Coriolis Force Couple*

The velocity is a sinusoidally varying function of the applied driving voltage versus time as given by Eq. (3), where θ_{max} represents the maximum proof mass angular displacement, ω is the drive voltage frequency, and *t* is time.

$$\theta(t) = \theta_{\max} \sin(\varpi t) \quad (3)$$

Using the small angle approximation, the angular displacement is converted to a linear displacement as given by Eq. 4, where r_{max} represents the distance measured from the proof mass center point to the mid point on the outer sense proof mass ring.

$$y_{\max} = \theta_{\max} r_{\max} \quad (4)$$

The angular displacement is converted to linear displacement along the y-axis, as given by Eq. 5, where the y_{max} represents the maximum displacement.

$$y(t) = \frac{y_{\max}}{2} \sin(\varpi t) \quad (5)$$

The velocity of the outer ring is defined by the time dervative of the position vector given by Eq. 6.

$$\frac{dy(t)}{dt} = \frac{y_{\max}}{2} \varpi \cos(\varpi t) \quad (6)$$

The peak velocity of the 44.96 [kHz] excited outer proof mass is 0.155 [m/s], with a corresponding Coriolis acceleration of 0.021 [m/s^2] for a 3.8 [deg/s] angular rate vector application as shown in Figure 4.

Parallel plate actuator arrays, as shown in Figure 5, were used to increase electrostatic force as compared to comb drive actuation for a fixed applied voltage at the expense of reduced proof mass deflection. The maximum proof mass linear deflection measured at the outer sense mass is approximately 1.1 [μm].

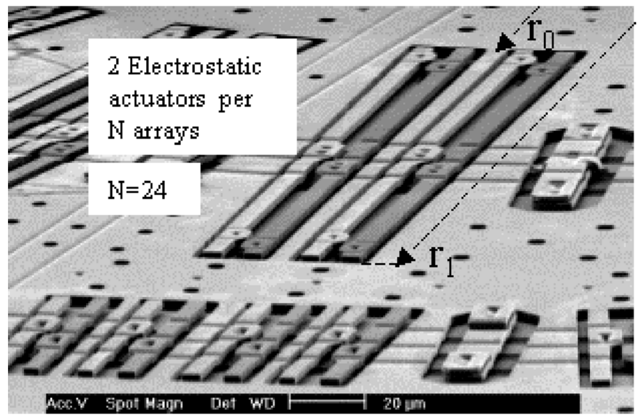

***Figure 5**. Parallel Plate Electrostatic Actuator Arrays*

The capacitance of the actuator array [**9**] is defined by Eq. 7., where *T* is the thickness of the proof mass, g_0 is the initial gap spacing, and r_0 and r_1 are measured distance from the proof mass center to inner and outer electrode radii as shown in Figure 5.

$$C(\theta) = \frac{2N\varepsilon_0 T}{\theta} \ln\left(\frac{g_0 - \theta r_0}{g_0 - \theta r_1}\right) \quad (7)$$

The angular derivative of the actuator array capacitance is given by Eq. 8.

$$\frac{dC(\theta)}{d\theta} = \frac{\varepsilon_0 T}{\theta}\left[\frac{r_1(g_0 - \theta r_0) - r_0(g_0 - \theta r_1)}{(g_0 - \theta r_0)(g_0 - \theta r_1)} - \frac{1}{\theta}\ln\left(\frac{(g_0 - \theta r_0)}{(g_0 - \theta r_1)}\right)\right] \quad (8)$$

The electrostatic torque generated by the parallel plate actuator arrays is defined by the angular derivative of the potential energy as given by Eq. 9, where V_θ represents the applied voltage amplitude.

$$\frac{dU_{cap}(\theta)}{d\theta} = \frac{1}{2}\frac{dC(\theta)}{d\theta} V_\theta^2 \quad (9)$$

Drive voltage amplitude was less than 4.6 [Volts] during sinusoidal proof mass excitation.

A cross section of a triply clamped beam used in the parallel plate electrostatic actuator array is shown in Figure 6.

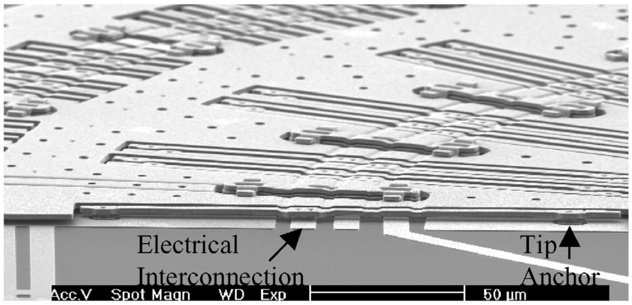

***Figure 6**. Electrostatic Actuator Array Triply Clamped Beam Cross Section*

Previous designs were anchored near the beam center at the underlying electrical polysilicon interconnection resulting in an 8X overall increase in the vertical spring constant as compared to cantilever beams of equal length, as shown in Figure 7.

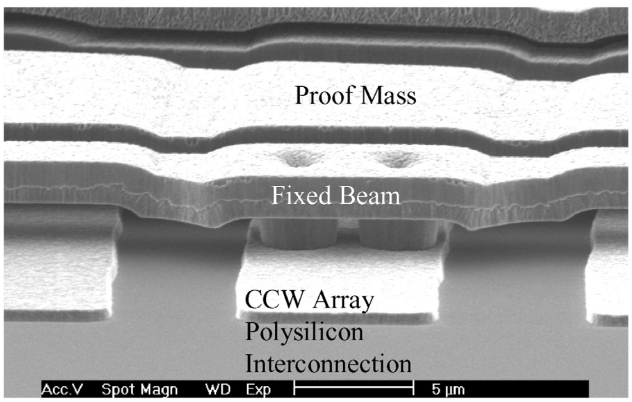

***Figure 7**. Centrally Anchored Parallel Plate Actuator Beams*

However, vertical stiction [**10**] was observed in arrays with beam lengths greater than 160µm during the sacrificial oxide etch process sequence. Centrally anchored beams shorter than 160µm were able to resist vertical stiction during processing and comprise the inner drive proof mass outer electrostatic actuator array as shown in Figure 5. Centrally anchored beams greater than 160µm in length were modified with tip support posts anchored to the substrate, as shown in Figure 8, to eliminate stiction by increasing the vertical spring constant by 128X as compared to simply supported cantilever beams of equal length.

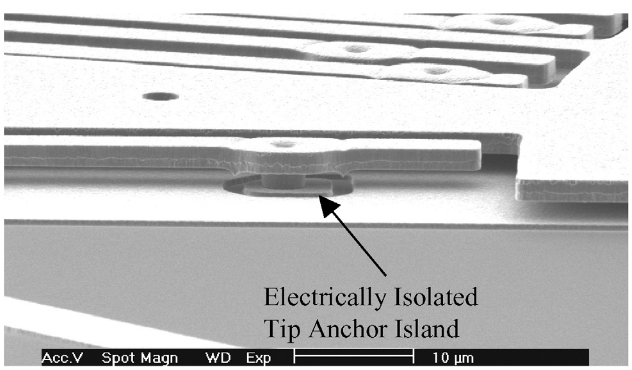

***Figure 8**. Triply Clamped Beam Tip Anchor Support*

SENSE ELECTRODE CONFIGURATION

Undesirable electrostatic coupling attributed to fringing electric field lines terminating on the top surface of the capacitive sensor [**11**] are eliminated using the differential capacitance electrode configuration as shown in Figure 9.

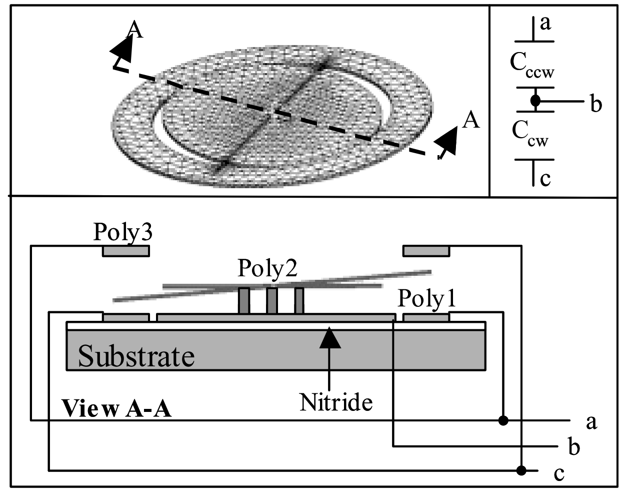

***Figure 9**. Differential Capacitance Electrode Configuration*

Each differential electrode covers one quarter of the outer proof mass area as shown in Figure 10.

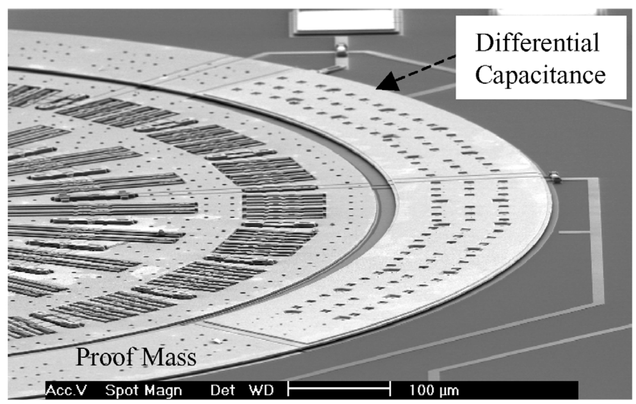

***Figure 10**. Differential Capacitance Sense Electrode*

Detail of the differential capacitance sense electrode is shown in Figure 11.

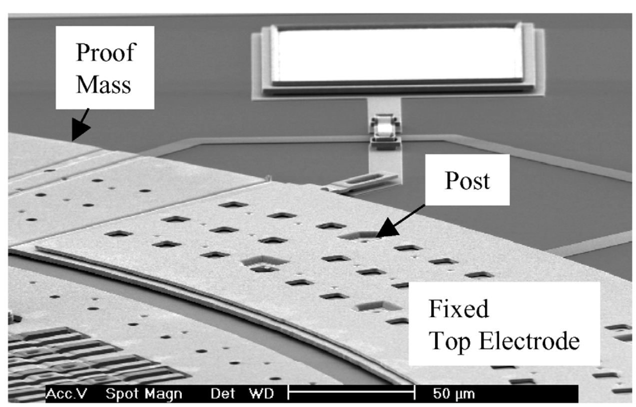

***Figure 11.** Differential Capacitance Sense Electrode Detail*

EXPERIMENTAL RESULTS

The resonant frequency of the sense proof mass mode was measured at 44.96 [kHz] in a 3 [mtorr] ambient using an HP 8751 Network Analyzer as shown in Figure 12.

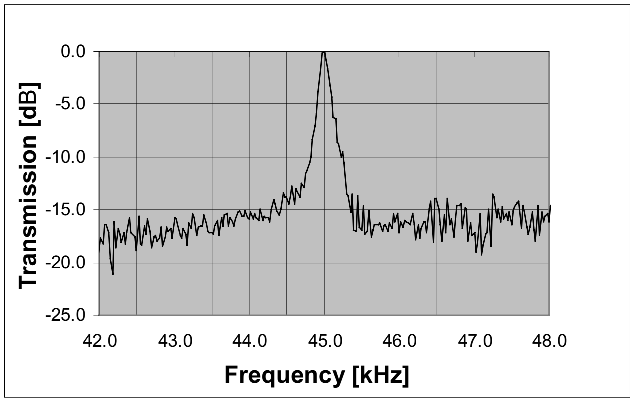

Figure 12. *Sense Mode Resonant Peak @44.96 [kHz], Q=225*

The quality factor Q=225 was extracted from the sense mass resonant frequency measurement, as given by Eq. 10, where the high and low –3dB frequency measurements were 45.02 [kHz] and 44.82 [kHz] respectively.

$$Q = \frac{F_0}{F_{-3dB\_HI} - F_{-3dB\_LO}} \qquad (10)$$

Angular rate resolution was measured in a 3 [mtorr] ambient as 3.8 [deg/sec] in a 20 [Hz] bandwidth, as shown in Figure 13, representing an 8.1 [mV/deg/sec] sensitivity.

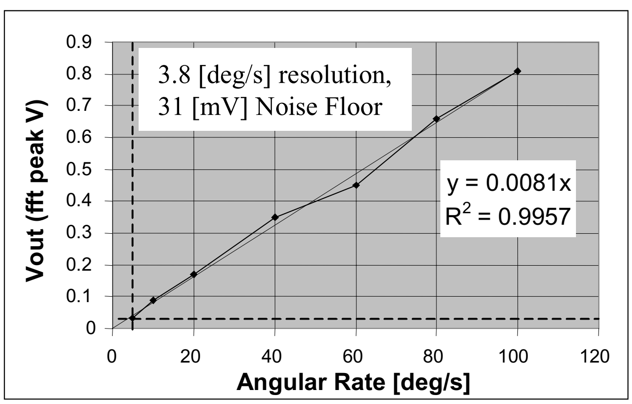

Figure 13. *Angular Rate Measurement*

CONCLUSION

We have demonstrated a low-cost high yield surface micromachined gyroscope with a decoupled drive and sense proof mass. A dual anchor approach is described using folded beam springs and a torsion post to significantly reduce undesired drive proof mass out of plane deflection while maintaining a comparatively low rotational mechanical restoring force. The Z-axis (vertical) proof mass suspension spring constant was increased from 7.86 [N/m] to 251 [kN/m] with the addition of the central torsion post. Interleaved springs attached at least two different radii can be used to supress precession of the central proof mass in lieu of the central torsion post. The interleaved support spring design scheme typically increases Z-axis spring constant by 2X while increasing the rotational spring constant by only 5-10%. Vertical stiction was eliminated from the design using the dual anchor scheme for the proof mass and a triply clamped beam approach for the fixed electrostatic drive/sense beams. The increase in the Z-axis spring constant of the fixed triply clamped beams is greater than 128X as compared to singly clamped cantilever beams of equal length. The parasitic capacitance of the fixed beam electrostatic arrays referenced to the silicon substrate is increased less than 16% due to the tip anchor inclusion. In addition, a differential capacitance measurement scheme is presented which rejects undesired proof mass linear acceleration error at the sensor. The differential capacitance electrode configuration also shields the sensor from fringing electrostatic fields allowing for increased angular rate sensitivity. The sense mode resonant frequency was measured at 44.96 [kHz] with a quality factor Q of 225 in a 3 [mtorr] ambient. Angular rate resolution was measured at 3.8 [deg/s] in a 20 [Hz] bandwidth with an 8.1 [mV/deg/s] sensitivity.

REFERENCES

1. M. W. Putty, and K. Najafi, "A Micromachined Vibrating Ring Gyroscope", Solid State Sensors and Actuators, Hilton Head, pp. 213-217, 1994.
2. A. Ayazi, and K. Najafi, "Design and Fabrication of a High Performance Polysilicon Ring Gyroscope", IEEE Micro Electromechanical Systems, pp. 621-626, 1998.
3. P. Greiff, B. Boxenhorn, T. King, and L. Niles, "Silicon Monolithic Gyroscope", Solid State Sensors and Actuators, Transducers 91, pp. 966-968, 1991.
4. J. Bernstein, S. Cho, A. T. King, A. Kourepenis, P. Maciel, and M. Weinberg, "A Micromachined Comb-Drive Tuning Fork Rate Gyroscope", IEEE Micro Electromechanical Systems, pp. 143-148, 1993.
5. M. Lutz, W. Golderer, J. Gerstenmeier, J. Marek, B. Malhofer, and D. Shubert, "A Precision Yaw rate Sensor in Silicon Micromachining", Solid State Sensors and Actuators, Transducers 97, pp. 847-850, 1997.
6. W. A. Clark, and R. T. Howe, "Surface Micromachined Z-Axis Vibratory Rate Gyroscope", Solid State Sensors and Actuators Workshop, Hilton Head, pp. 283-287, 1996.
7. T. Juneau, A. Pisano, and J. H. Smith, "Dual Axis Operation of a Micromachined Rate Gyroscope", Solid State Sensors and Actuators, Transducers 97, pp. 883-886, 1997.
8. W. Geiger, B. Folkmer, J. Merz, H. Sandmaier, and W. Lang, "A New Silicon Rate Gyroscope", IEEE Micro Electromechanical Systems, pp. 615-620, 1998.
9. G. J. O'Brien, D. J. Monk, and L. Lin, "MEMS Cantilever Beam Electrostatic Pull-in Model", SPIE MEMS, Vol. 4593, pp. 31-41, 2001.
10. C. H. Mastrangelo and C. H. Hsu, "Mechanical Stability and Adhesion of Microstructures Under Capillary Forces –Part 1: Basic Theory", Journal of MicroElectromechanical Systems, Vol. 2, No. 1, 1993.
11. W. Tang, M. G. Lim, and R. T. Howe, "Electrostatic Comb Drive Levitation and Control Method", Journal of Micro Electromechanical Systems, Vol. 1, No. 4, 1992.